Hysteresis Phenomena in Perovskite Solar Cells: the Many and Varied Effects of Ionic Accumulation -

Supplementary Information

Experimental

Cell Fabrication: The measurements reported in Figs. 1,4,5,6,7 were performed on cells with a mesoporous structure (FTO/compact-TiO2/ mesoporous-TiO2/CH3NH3PbI3/spiro-OMeTAD/Au). The PVSCs were fabricated on FTO glass substrates (TEC7, DYESOL, with sheet resistance of 7 Ω sq−1), which were cleaned separately in acetone, isopropanol, and ethanol for 30 min each in an ultrasonic bath, and then dried in nitrogen gas. Compact layers were prepared by either a spin-coating processes or via atomic layer deposition (ALD). For the solution-deposited compact layer 50 nm of TiO2 was deposited on the substrates via spin coating at 2000 rpm for 45 s from a precursor solution consisting of (350 µL) titanium isopropoxide and HCl (35 µL, 2 M) in anhydrous Et-OH (5 mL). Alternatively a $TiCl_4$ source was used to run atomic layer deposition at 250°C to achieve a compact layer with the same (50nm) thickness. The substrates with compact layer were then sintered in the furnace in air for 30 min at 500 °C. To develop the ≈200 nm thick mesoporous layer a TiO2 paste (30 NR-D, Dyesol) with an average particle size of 30 nm diluted in anhydrous Et-OH (1:5 by weight) was spin coated for 40 s at 5000 rpm with a ramp of 500 rpm s−1 . After spin coating, the samples were immediately dried at 100 °C for 10 min on a hotplate and sintered in the furnace at 500 °C for 30 min in air. All the following processes were performed inside a glovebox. CH3NH3PbI3 was prepared using the halide precursors (PbI2 1 M and CH3NH3I 1 M, Sigma-Aldrich) dissolved in mixed solvent of N,N- dimethylformamide (0.7 mL, DMF, Sigma-Aldrich) and dimethylsulfoxide (0.3 mL, DMSO, Sigma-Aldrich). The perovskite precursor was then spin coated onto the substrate at 5000 rpm for 60 s. During the spin-coating, chlorobenzene (50 µL, Sigma-Aldrich) was dropped onto the center of the substrate after spinning started for 10 s. The spin- coated film was annealed at 100 °C for 15 min on the hotplate and then left to cool in the Petri dish. The spiro-OMeTAD solution was spin-coated at 4000 rpm for 40 s onto the perovskite film to form the HTL. The spiro-OMeTAD precursor solution and film preparation were prepared as described in ref. 1[1]. Finally, a 100 nm gold contact layer was thermally evaporated onto the rear of the device.

Characterization: I–V measurements were carried out within a measurement stage that provided a low vacuum (15 psi) environment for the cell. The cell was un-encapsulated and in direct contact with the anodized aluminium base of the jig, which was temperature controlled at 25 °C. A solar simulator (PET SS150) was used and the cell was illuminated with light approximating the AM 1.5G spectrum at 1 sun intensity (100 mW cm^{-2}).

Efficiencies: The cells fabricated for this study were designed to represent a standard test structure (FTO/compact-TiO2/ mesoporous-TiO2/CH3NH3PbI3/spiro-OMeTAD/Au) instead of being optimized for high performance. We estimate stabilized efficiencies in the range of 10-13% for the cells reported in Figs. 1,4,5,6 and 7 on the basis of forward/reverse sweeps taken at intermediate rates as in Fig 1(b).

SCAPS: The recombination model in SCAPS[2] can include contributions from SRH centres in the bulk and at interfaces, as well as radiative and Auger recombination. The SRH parameters used in our model are included in table S1, whereas the other two recombination mechanisms were effectively disabled. The mesh in SCAPS is automatically generated by specifying upper limits on the solution's element-to-element variation, and was generally less than 0.1 nm in sensitive regions of the cell for most of our calculations.

Accumulation Model

To produce the simulations presented in the main text the ionic accumulation was assumed to occur in homogenous accumulation zones of fixed width. Since it is still uncertain which ions are the dominant movers in $MAPbI_3$, and along which pathways they diffuse through the material, we believe that this simplification is justified. Here for completeness we compare the predictions of this simplified model with that of the drift-diffusion approach used in other recent work.[3,4]

The drift-diffusion equation predicts sharp accumulation zones and wider depletion zones which grow with the mobile ion density as shown in Fig. S2(a). Whether accumulation occurs on one side of the cell or the other

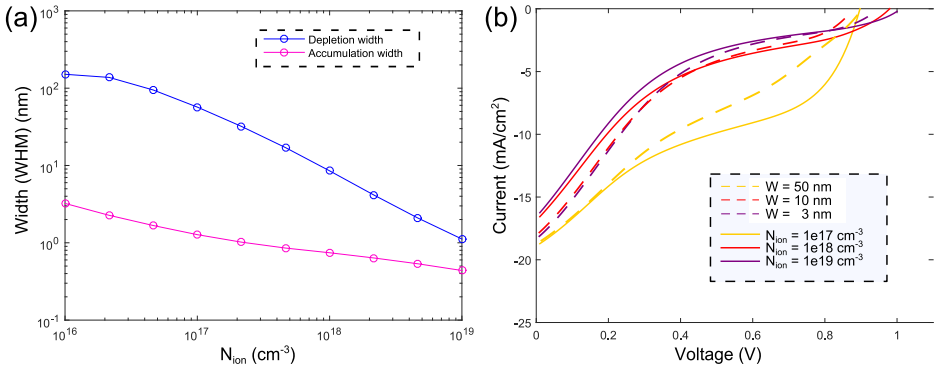

Figure S1: Comparison of different models of ion accumulation. (a) Simulated fast-forward scans after 0V pre-bias using the homogeneous accumulation region approximation used in the main text (dotted lines) and the drift-diffusion equation (solid). (b) Simulated reverse scans under high positive accumulation (equivalent to a 1.5V pre-biasing period) as in Fig. 5 of the main text, but with different choices for the accumulation width W.

depends on the charge of the mobile species. To remove the complication of this asymmetry we consider accumulation and depletion within zones of equal width. As in Fig. 2(a) of the main text, Fig. S2(b) shows rapid-forward scan IV curves simulated after equilibrating the cell at 0V, using both the drift-diffusion and homogeneous layer approximations. These results indicate that qualitative characteristics of the forward scan are mostly unaffected by the choice of accumulation model. Note that the ion density quoted in the figure corresponds to an average concentration, and that higher concentrations correspond to narrower accumulation widths as discussed in[4] and the main text. It can be seen in the figure that the characteristics for the highest density using drift-diffusion qualitatively correspond to those of the narrowest width using our approximation, and vice versa.

S-shaped rapid scans and surface recombination

In the main text we claim that surface recombination at both interfaces and ionic accumulation combine to result in the S-shaped rapid scans reported in Fig 4. The simulated results in Fig. 4b demonstrate that the negative accumulation resulting from pre-bias voltages near 0V are one necessary feature. Here in Fig. S4a we show that surface recombination is also necessary by calculating the same curves with fixed ion accumulation and varying interfacial recombination velocities. Surface recombination plays an almost equally important role in the inverse hysteresis effect as illustrated in Fig. S3b.

Inverse Hysteresis, additional measurements

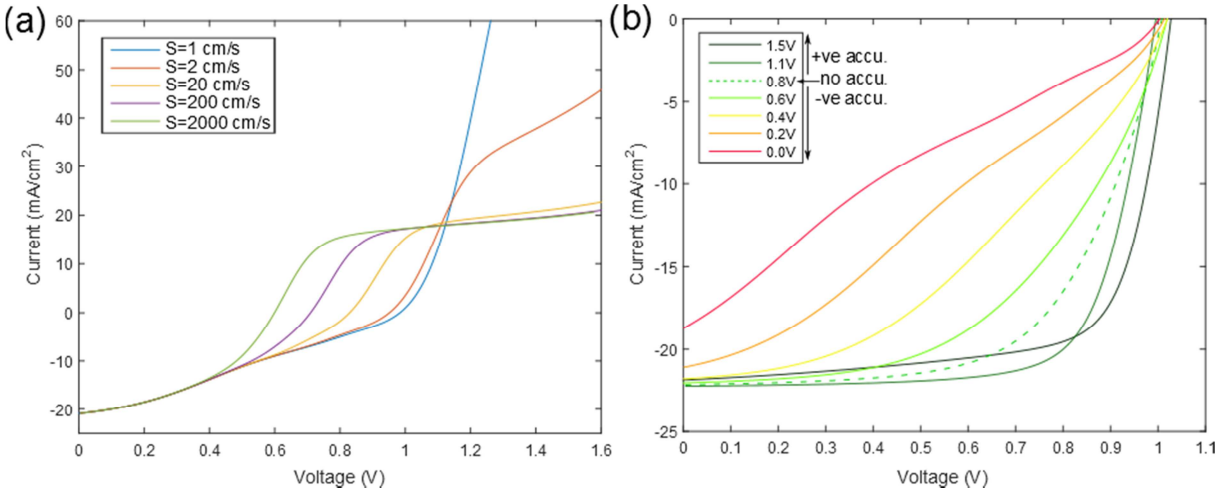

Figure S2: (a) Simulated rapid scans up to high forward bias as in Fig 4 of the main text, but this time under constant ionic accumulation (0V pre-bias) but varying levels of surface recombination (set equal at both interfaces). The results show that significant surface recombination is necessary to see the S-feature. (b) Simulated rapid scans as in Fig. 5, but with reduced surface recombination, showing a smaller reduction in J_{sc} following forward-biasing (reduced inverse hysteresis) and less impact on the open-circuit voltages under negative accumulation.

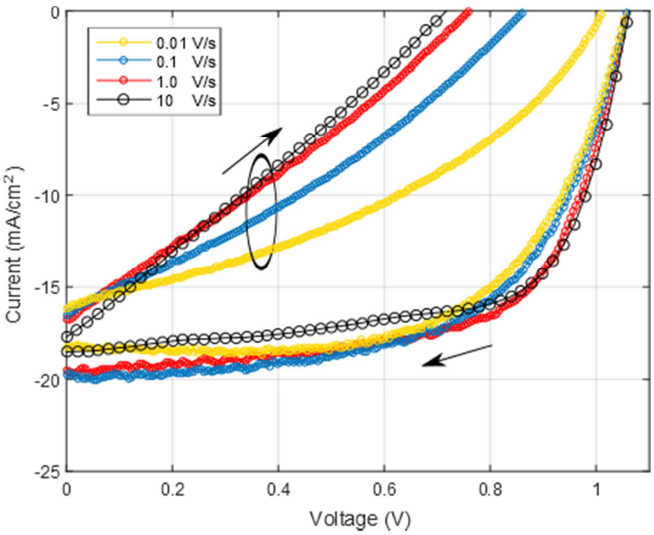

Figure S3: A reproduction of the measurements in Fig. 1(b) of the main text on a cell exhibiting inverse hysteresis , evident here as lowered J_{sc} on the rapid reverse scans. Once again the scans are taken after pre-biasing at short-circuit for the forward scan and the stabilized open-circuit voltage for the reverse scans. We attribute the reduced J_{sc} on the rapid reverse scans (10V/s) to positive accumulation, and the reduced J_{sc} for the slowest scan (0.01V/s) to negative accumulation, as in the rapid forward scans.

As in Fig. S1(a), the forward scans (following 0V pre-bias) are found to exhibit unusual shapes for some parameter choices, evoking two distinct fill factors. Some cells exhibit these shapes in experiment (e.g. Fig S4a), although it is not clear at this stage why others display a more linear trend as in Fig. 1a. In our model these unusual rapid scans can be traced to the effect of extreme carrier build-up at forward bias caused by negative ionic accumulation. Becoming more severe at forward bias, the build-up of carriers eventually reaches the point where carrier-screening of the applied bias occurs. Beyond this point the applied potential drops over the interface layers rather than the perovskite itself (Fig. S4(b)). This can be verified by observing that the effect vanishes at lower illumination intensities under which carrier densities are smaller and the expected linear increase of electric field with applied bias re-emerges (Fig. S4(c)). The appearance of two separate fill factors in these curves can therefore be understood as indicating that the applied bias is dropping in different regions of the cell, first within the absorber bulk and then over the interface heterojunctions as the bias voltage is increased.

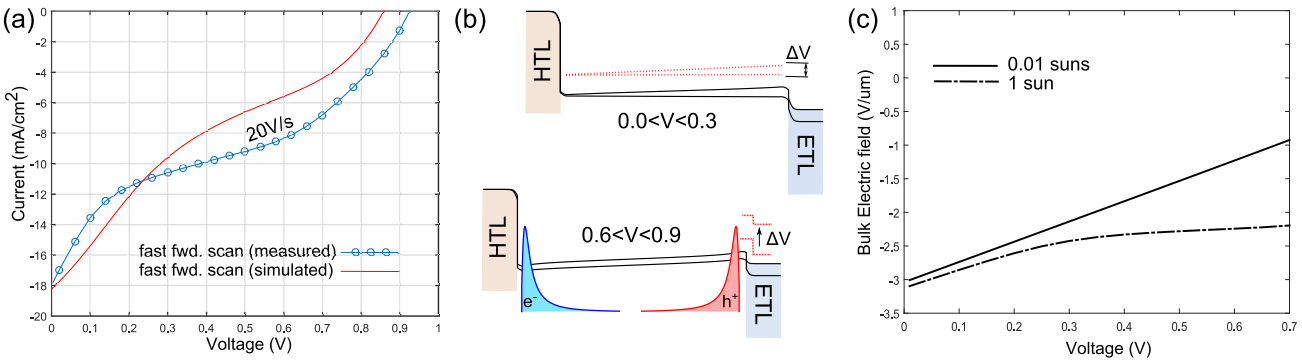

Figure S4: (a) Measured and simulated fast forward scans after 0V pre-bias exhibiting unusually shaped IV curves which evoke two distinct fill factors. (b) Band diagrams taken from simulation illustrating that the applied potential drops over different regions of the cell at different bias voltages due to the carrier build-up caused by negative ionic accumulation. (c) Bulk electric field versus bias voltage in a cell with negative ionic accumulation under low and standard illumination, providing further evidence that carrier build-up is responsible for screening the applied potential.

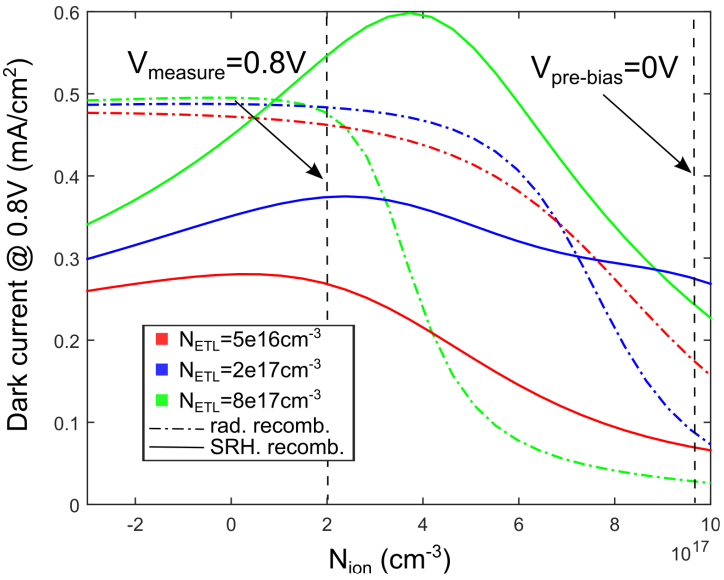

Figure S5: Simulated dark current at a bias of 0.8V for cells with different modes of recombination: bulk SRH (solid line) and radiative (dotted line), indicating that non-monotonic dependence occurs only with SRH recombination. Differing trends for different values of the ETL doping show that details of interface layers may determine whether or not a non-monotonic current dependence occurs in a given cell. Here W was set to 30nm.

Non-monotonic dark current as evidence for trap-saturation

As discussed in the main text we find that some cells exhibit non-monotonic transient behaviour when subjected to a change in bias voltage in the dark. This was attributed to the effect of trap-filling and a switch-over in the limiting carrier for recombination. Figure S5 shows the simulated dark current (measured at 800mV) at different levels of ionic accumulation for cells with different interface layers and subject to either SRH or purely radiative recombination. In the transient measurements and simulations of Fig. 7 in the main text the ions begin in the state labelled as 0V and relax to the position labelled 0.8V over the course of the measurement. It can be seen that only cells with SRH recombination exhibit non-monotonic behaviour, supporting our hypothesis that this comes about due to the existence of a limiting carrier for recombination which switches from holes to electrons (or vice versa) as a function of accumulation. Model Parameters

The primary model parameters used for all simulations presented in the main text are given below in table S1. The values without citations are estimates unless otherwise stated. It should be noted that the true energy alignments at the perovskite interfaces are still significantly uncertain[10]. All the SRH defect parameters given in table S2 represent estimates which resulted in approximate agreement with the characterization experiments of the main text.

	E_g (eV)	χ (eV)	μ_n ($cm^2V^{-1}s^{-1}$)	μ_p ($cm^2V^{-1}s^{-1}$)	N_c (cm^{-3})	N_v (cm^{-3})	$width$ (nm)	$N_A - N_D$ (cm^{-3})	ϵ_r
ETL (TiO_2)	3.0	4.15*	0.01†	2‡	1E20 cm^{-3}	1E20 cm^{-3}	50	1E16[e],5E17[d],1E18[a,b,c]	31 [5]
ABS ($MAPbI_3$)	1.55[6]	3.9*	2	2	2E18 cm^{-3} [7]	2E19 cm^{-3} [7]	320	-	18 [8]
HTL (Spiro)	3.0	2.2*	0.01	2‡	1E20 cm^{-3}	1E20 cm^{-3}	200	5E17[d],1E18[a,b,c],1.5E18[e]	3[9]

*These values were chosen to symmetrize the band offsets at the Spiro/$MAPbI_3$ and $MAPbI_3$/TiO_2 interfaces for simplicity.

†This parameter should represent an effective mobility for the combined mesoporous-compact TiO_2 layer.

‡The neglect of absorption in the transport layers makes these minority carrier mobilities of little to no importance.

	Location	Density (cm^{-3}/cm^{-2})	σ_n (cm^{-2})	σ_p (cm^{-2})	Type	E_t
Defect 1	ETL/ABS	0[d],1E7[a],1E8[e],1E9[b],1E10[a,c]	1E-13[b],1E-15[a,c,d,e]	1E-15	Neutral	$E_v^{HTL} + 0.6$ eV
Defect 2	ABS	0[d],1E16[a,b,c],2E16[e]	1E-15	1E-15	Neutral	$E_v^{ABS} + 0.6$ eV
Defect 3	ABS/HTL	1E7[a],1E9[b,d],1E10[a,c],5E10[e]	1E-15	1E-13[b],1E-15[a,c,d,e]	Neutral	$E_v^{ABS} + 0.6$ eV

a,b,c,d,e: Parameter choices specific to the models of figures 3,4,5,6,7 respectively.

Table S1: Primary model parameters used for the results presented in the main text.

References

1 D. Liu and T. L. Kelly, *Nat. Photonics*, 2013, **8**, 133–138.

2 M. Burgelman, P. Nollet and S. Degrave, *Thin Solid Films*, 2000, **361**, 527–532.

3 S. Van Reenen, M. Kemerink and H. J. Snaith, *J. Phys. Chem. Lett.*, 2015, **6**, 3808–3814.

4 G. Richardson, S. O'Kane, R. G. Niemann, T. Peltola, J. M. Foster, P. J. Cameron and A. Walker, *Energy Environ. Sci.*, 2016, **9**, 1476–1485.

5 H. Tang, K. Prasad, R. Sanjines, P. E. Schmid and F. Levy, *J. Appl. Phys.*, 1994, **75**, 2042–2047.

6 M. M. Lee, J. Teuscher, T. Miyasaka, T. N. Murakami and H. J. Snaith, *Science*, 2012, **338**, 643–7.

7 Q. Zhou, D. Jiao, K. Fu, X. Wu, Y. Chen, J. Lu and S. E. Yang, *Sol. Energy*, 2016, **123**, 51–56.

8 M. Samiee, S. Konduri, B. Ganapathy, R. Kottokkaran, H. a. Abbas, A. Kitahara, P. Joshi, L. Zhang, M. Noack and V. Dalal, *Appl. Phys. Lett.*, 2014, **105**, 2012–2016.

9 D. Poplavskyy and J. Nelson, *J. Appl. Phys.*, 2003, **93**, 341–346.

10 S. Olthof, *APL Mater.*, 2016, **091502**.